Nightside Neutral Density Disturbances Collocated With Equatorial Plasma Irregularities Above 450 km

GRACE and GRACE-FO Observations in 2002–2022

Song, Hosub; Park, Jaeheung; Xiong, Chao; IJssel, Jose van den; Lee, Daehee; Lee, Jaejin; Yi, Yu

DOI
10.1029/2023SW003851

Publication date
2024

Document Version
Final published version

Published in
Space Weather

Citation (APA)
Song, H., Park, J., Xiong, C., IJssel, J. V. D., Lee, D., Lee, J., & Yi, Y. (2024). Nightside Neutral Density Disturbances Collocated With Equatorial Plasma Irregularities Above 450 km: GRACE and GRACE-FO Observations in 2002–2022. *Space Weather*, *22*(12), Article e2023SW003851. https://doi.org/10.1029/2023SW003851

Space Weather

RESEARCH ARTICLE
10.1029/2023SW003851

Nightside Neutral Density Disturbances Collocated With Equatorial Plasma Irregularities Above 450 km: GRACE and GRACE-FO Observations in 2002–2022

Hosub Song[1], Jaeheung Park[1,2], Chao Xiong[3], Jose van den IJssel[4], Daehee Lee[1], Jaejin Lee[1], and Yu Yi[5]

[1]Space Science Division, Korea Astronomy and Space Science Institute (KASI), Daejeon, South Korea, [2]Department of Astronomy and Space Science, University of Science and Technology (UST), Daejeon, South Korea, [3]Department of Space Physics, Electronic Information School, Wuhan University, Wuhan, China, [4]Faculty of Aerospace Engineering, Delft University of Technology, Delft, The Netherlands, [5]Department of Astronomy, Space Science and Geology, Chungnam National University (CNU), Daejeon, South Korea

Abstract We investigate the climatology of Neutral Density Disturbances (NDDs) collocated with Equatorial Plasma Irregularities (EPIs) at altitudes above 450 km by using 20 years of data from the Gravity Recovery and Climate Experiment (GRACE) and GRACE-FO satellites. Electron density data are used to detect EPIs, and thermospheric neutral density measured onboard the same spacecraft serves to identify EPI-related NDDs. A detailed analysis focused on the morphological similarity between electron and neutral densities. To examine the relationship between EPI and NDD, statistical dependences of EPIs and NDDs on season/longitude (S/L), Magnetic Latitude (MLAT), Magnetic Local Time (MLT), and solar activity have been checked. As a first step, we confirmed that the EPI climatology in GRACE satellite data is consistent with previous reports. Then, it is found that the lower the neutral density in the background upper thermosphere, the higher the probability that EPI can accompany NDDs. We suggest that the vertical plasma advection surrounding EPI can result in neutral density disturbance, of which the efficiency depends on the background neutral scale height or temperature. The colder the thermosphere, the shorter its vertical scale height (or the lower the background neutral density), which can make the plasma advection leave measurable imprints on the neutral density.

Plain Language Summary In this paper, we analyze the association between Equatorial Plasma Irregularities (EPIs) and Neutral Density Disturbances (NDDs) at altitudes above 450 km, which has been seldom investigated before. EPIs are electron density irregularities in the nightside equatorial and low-latitude ionosphere, and they are known to disturb the surrounding thermospheric neutral density, causing the NDD. The relationship between EPI and NDD has been analyzed previously, but very few investigations were based on simultaneous measurements of electron and neutral densities. In this study, with GRACE/GRACE-FO satellites measuring electron and neutral density from the same platform, we investigate the relationship between the two phenomena more quantitatively. The statistical dependences of EPIs and NDDs on season/longitude (S/L), Magnetic Latitude (MLAT), Magnetic Local Time (MLT), and solar activity are studied. One interesting finding is that the lower the background neutral density in the upper thermosphere, the higher the probability of EPI accompanying measurable NDDs.

Key Points:

- Neutral density disturbances (NDDs) associated with equatorial plasma irregularities (EPIs) are investigated at altitudes above 450 km
- NDDs are conservatively identified by correlating neutral and plasma density profiles measured onboard the same spacecraft
- The lower the background neutral density, the higher the probability of EPI accompanying measurable NDD

Correspondence to:
H. Song,
hssong@kasi.re.kr

Citation:
Song, H., Park, J., Xiong, C., IJssel, J. v. d., Lee, D., Lee, J., & Yi, Y. (2024). Nightside neutral density disturbances collocated with equatorial plasma irregularities above 450 km: GRACE and GRACE-FO observations in 2002–2022. *Space Weather*, *22*, e2023SW003851. https://doi.org/10.1029/2023SW003851

Received 30 DEC 2023
Accepted 23 SEP 2024

Author Contributions:
Data curation: Hosub Song
Formal analysis: Hosub Song, Jose van den IJssel
Funding acquisition: Daehee Lee, Jaejin Lee
Investigation: Hosub Song
Methodology: Hosub Song, Jaeheung Park
Project administration: Jaeheung Park
Resources: Hosub Song
Software: Hosub Song
Supervision: Jaeheung Park, Chao Xiong, Daehee Lee, Jaejin Lee, Yu Yi
Validation: Jaeheung Park, Chao Xiong, Daehee Lee, Jaejin Lee, Yu Yi
Writing – original draft: Hosub Song
Writing – review & editing: Hosub Song, Jaeheung Park, Chao Xiong, Jose van den IJssel, Yu Yi

1. Introduction

Equatorial plasma Irregularities (EPIs) signifies electron density irregularities in the nightside equatorial and low-latitude ionospheric F-region (Aa et al., 2020; Burke et al., 2004; F. Huang et al., 2021; Kil, 2015; Kuai et al., 2022; Park et al., 2008; Park, Mende, et al., 2022; Xiong et al., 2010). The EPI can originate from the bottom side of the F-layer where the background plasma density increases with height, which can become unstable due to Rayleigh-Taylor instability after sunset (Kelley, 2009; Kil, 2022; Wu et al., 2020). It is known that the evening pre-reversal enhancement of the upward plasma drift can expedite the instability process (Fejer et al., 1999; Park et al., 2008; Whalen, 2003; Xiong et al., 2016). EPIs are frequently encountered and have a relatively higher occurrence rate at American-Atlantic-African longitudes, and their occurrence increases as solar activity goes up (C. S. Huang et al., 2014; C. Y. Huang et al., 2002; Stolle et al., 2006; Xiong et al., 2010).

Neutral density disturbances (NDDs), phenomenon in which thermospheric mass density is locally disturbed in low magnetic latitudes, were first observed in 1998 through the San Marco V satellite data, and it was suggested that the NDDs might be created by EPIs (Illés-Almár et al., 1998; Park et al., 2010). However, the San Marco V satellite did not cover the entire globe, focusing only on the equatorial region due to its 3° inclination (Bencze et al., 2000). In addition, the mission lifetime was very short, only from April to December of 1988, so the data are not appropriate for studying seasonal variation and solar cycle effects of NDDs. Also, the NDD climatology using San Marco V mainly focused on altitudes lower than 350 km (Park et al., 2010). So, Park et al. (2010) studied the relationship between EPI and NDD using the Challenging Minisatellite Payload (CHAMP) satellite to overcome these limitations. Launched on 15 July 2000, the CHAMP satellite operated in a circular near-polar orbit at an initial altitude of ∼450 km, and with an inclination of 87°. The operation was terminated at an altitude of ∼300 km on 19 September 2010. For this reason, the CHAMP satellite allows NDD research to be conducted at a wider latitude range, longer data periods, and higher altitudes than the San Marco V satellite.

However, there is still room for improvement in studying the details between EPIs and NDDs. First, NDD statistics at a higher altitude than CHAMP are warranted. The most extensive statistics until now were reported for 2002–2005 by Park et al. (2010), which used CHAMP satellite data below ∼420 km. As for the NDDs above ∼420 km, only the existence (e.g., Illés-Almár et al., 1998) and rarity (e.g., Bencze et al., 2000; Figure 8) were reported until now; furthermore, both of the above-mentioned papers used San Marco V satellite observations and are therefore only relevant to near-equatorial regions. No dedicated global (i.e., including off-equatorial) climatology is known above 450 km altitude. Fortunately, Gravity Recovery and Climate Experiment (GRACE) and GRACE Follow-On (GRACE-FO) have collected both the neutral and electron density data around 500 km.

Second, electron density data at a faster sampling rate than for CHAMP are needed for robust identification of "EPI-related" NDDs. Bencze et al. (2000) seems to make no use of plasma density data for solidifying NDD identification. Park et al. (2010) only used magnetic field data with a 1 Hz sampling rate to confirm that the neutral density perturbations (0.1 Hz) are due to plasma irregularities, that is, the existence of EPI around NDD was not directly confirmed by plasma density data due to its low sampling rate (1/15 Hz), but only indirectly inferred from magnetic field changes (Stolle et al., 2006). Because here we identify NDDs based on the morphological similarity between electron and neutral density profiles, the event list can be robust against (a) possible noise in the accelerometer data or (b) neutral density fluctuations coming from other sources (e.g., gravity waves). The good news is that electron density measurements by GRACE and GRACE-FO have a better temporal resolution: that is, three times finer than CHAMP data (5 vs. 15s) and two times finer than the neutral density data (5 vs. 10s). The higher resolution allows us to directly compare ion and neutral density profiles. Based on their morphological similarity (i.e., correlation coefficients), more rigorous and conservative identification of "EPI-related" NDDs is possible with GRACE and GRACE-FO, which has not been endeavored in previous studies.

Third, data covering nearly two solar cycles are valuable to evaluate the solar activity dependence of NDD, as neither San Marco V nor CHAMP data could cover such a long period. To deal with these issues, we will use the GRACE and GRACE-FO satellites, which together cover a much longer period (2002–2022). With a large amount of data, the resultant statistics can be more consolidated and reliable than could be attained previously.

Based on the three rationales mentioned above, we investigate the climatology of EPIs and NDDs at altitudes between 450 and 500 km. Section 2 is dedicated to descriptions of the spacecraft, scientific payloads, and data processing methods. Section 3 presents statistical distributions of EPIs and NDDs, which are discussed in Section 4. Finally, Section 5 summarizes the main findings and draws conclusions.

2. Satellites and Data Processing Methods

2.1. GRACE and GRACE-FO Satellite and Instrument

The GRACE satellites were launched on 17 March 2002 as a fleet of two satellites, GRACE-A and GRACE-B (Tapley et al., 2004). They were in a polar orbit with an inclination angle of 89° and can cover all Local Times (LTs) within 160.5 days (Xiong et al., 2010). The initial altitude of the GRACE satellites is ∼500 km, which was poorly explored by previous NDD studies (Park et al., 2010; C Xiong et al., 2010). After the GRACE mission successfully ended in October 2017, the GRACE-FO satellites, consisting of GRACE-C and GRACE-D were launched as a follow-up mission on 22 March 2018. GRACE-FO is also in a polar orbit at an inclination of 89° and an altitude of ∼500 km (Landerer et al., 2020; Park et al., 2020; Schreiter et al., 2023).

GRACE and GRACE-FO are equipped with a K-Band Ranging (KBR) system developed by the Jet Propulsion Laboratory to accurately measure the inter-satellite distance (Kim & Lee, 2009). The two GRACE (or GRACE-FO) satellites are following each other on the same orbit (Xiong et al., 2021), and their inter-spacecraft range observations can be used to derive the average plasma density between the two GRACE spacecraft (Xiong et al., 2010). The KBR measures the Total Electron Content using the carrier phase in the K (26 GHz) and Ka (32 GHz) bands (Schreiter et al., 2023; Yan et al., 2021), which is divided by the inter-spacecraft distance to yield average *Ne* (Xiong et al., 2015). While the CHAMP satellite was equipped with a Planar Langmuir Probe that produces electron density data every 15 s, the KBR of GRACE generates similar data every 5 s, providing better time resolution (C Xiong et al., 2010). Both CHAMP and GRACE (and GRACE-FO) satellites have 3-axis accelerometers to measure the total non-gravitational accelerations acting on the satellites, due to for example, atmospheric drag (Behzadpour et al., 2021; Christophe et al., 2015; Klinger & Mayer-Gürr, 2016). These observations have been used to derive in situ neutral mass density (ρ) and crosswind observations (Park et al., 2023; Siemes et al., 2023). In this study, we use the neutral mass density of GRACE-A and GRACE-C, which are available with a 10-s sampling. The neutral mass density data of GRACE-B is largely redundant for statistical studies with GRACE-A due to the small inter-satellite distance, and no neutral mass density is available for GRACE-D due to accelerometer issues (Behzadpour et al., 2021).

2.2. Data Processing Methods

The coverage of GRACE/GRACE-FO satellite plasma and neutral mass density data used in this paper is from 4 April 2002 to 29 April 2022, which corresponds to approximately 20 years of data. Only the GRACE/GRACE-FO data at altitudes above 450 km were used during this period, to distinguish our results from those of CHAMP. In addition, we focus on geomagnetically quiet-time climatology and only use data with a Kp index of less than 3 (Matzka et al., 2021; Xiong et al., 2010). First, for all *Ne* and ρ data, the Magnetic Latitude (MLAT) and Magnetic Local Time (MLT) are calculated using the Apexpy software package (Emmert et al., 2010; van der Meeren et al., 2023). We focus on the data whose absolute value of the MLAT (called |MLAT|) is less than 25°, and whose MLT is at nighttime between 18:00 and 04:00. Note that EPIs sometimes can extend beyond 25 degrees of MLAT, but that kind of events do not often occur (e.g., Stolle et al., 2006). This procedure leads to a discrete time-series of data points, each of which spans −25° MLAT and +25° MLAT at night. We further cut each of those time-series at the magnetic equator, and the result (i.e., northern or southern half) is used as a basic unit of the following climatology and called "segment." For example, for one complete orbit of GRACE, usually 2 nightside segments are obtained: one in the Northern Hemisphere (NH) and the other in the Southern Hemisphere (SH).

We note that GRACE(-FO) *Ne* and ρ data are produced by different payloads. The sampling rate is 5 s for *Ne* and 10 s for ρ data, and the two data sets are asynchronous. Therefore, the data should be intentionally synchronized at a cadence of 10.0 s through interpolation. Then, a Savitzky-Golay filter (window length is 7 data points or 70 s, and polynomial order is 2) is applied to each segment of *Ne* and ρ data, which is equivalent to a low-pass filtering. The difference between raw data and low-pass filter results is considered as residuals (ΔNe and $\Delta\rho$), which represent spatial inhomogeneity of electron and neutral density and are the focus of this paper. We further calculate the correlation coefficient between ΔNe and $\Delta\rho$ for robust identification of EPI-related NDDs. Specifically, the peak with the highest $|\Delta Ne|$ (i.e., the strongest plasma irregularity) within a "segment" is detected, ±70 s of the surrounding region is selected, and the correlation coefficient between ΔNe and $\Delta\rho$ is obtained in this selected region.

Figure 1 shows an example of GRACE data around 00:41 coordinated universal time (UTC) on 24 September 2002, which consists of two "segments" of electron and neutral density: one in the SH (left-hand side) and the other in the NH (right-hand side). The *x*-axis is Geographic Latitude (GLAT) and also includes the MLAT scale below. A black dotted line in the middle of all the panels signifies the magnetic equator. In panel (a), the black dots are electron densities measured by GRACE/KBR, and the background trend obtained by the Savitzky-Golay filter is a red dotted line. Panel (b) shows the residual (ΔNe) between the raw electron density of panel (a) and the Savitzky-Golay fitting. The standard deviation of the absolute value of ΔNe for each "segment" (or for each hemisphere) is written at the bottom of the panel (b). The ±70 s intervals used for correlation analysis are highlighted with a solid blue line in panel (b), which represents regions around the maximum $|\Delta Ne|$ position. Panels (c) and (d) are similar to panels (a) and (b), but show neutral densities and their residuals (ρ and $\Delta\rho$). The correlation coefficient (R) is written on the upper end of panel (d): the high correlation coefficients indicate a close resemblance between the blue solid lines (i.e., residuals or inhomogeneities) of panels (b) and (d). In panel

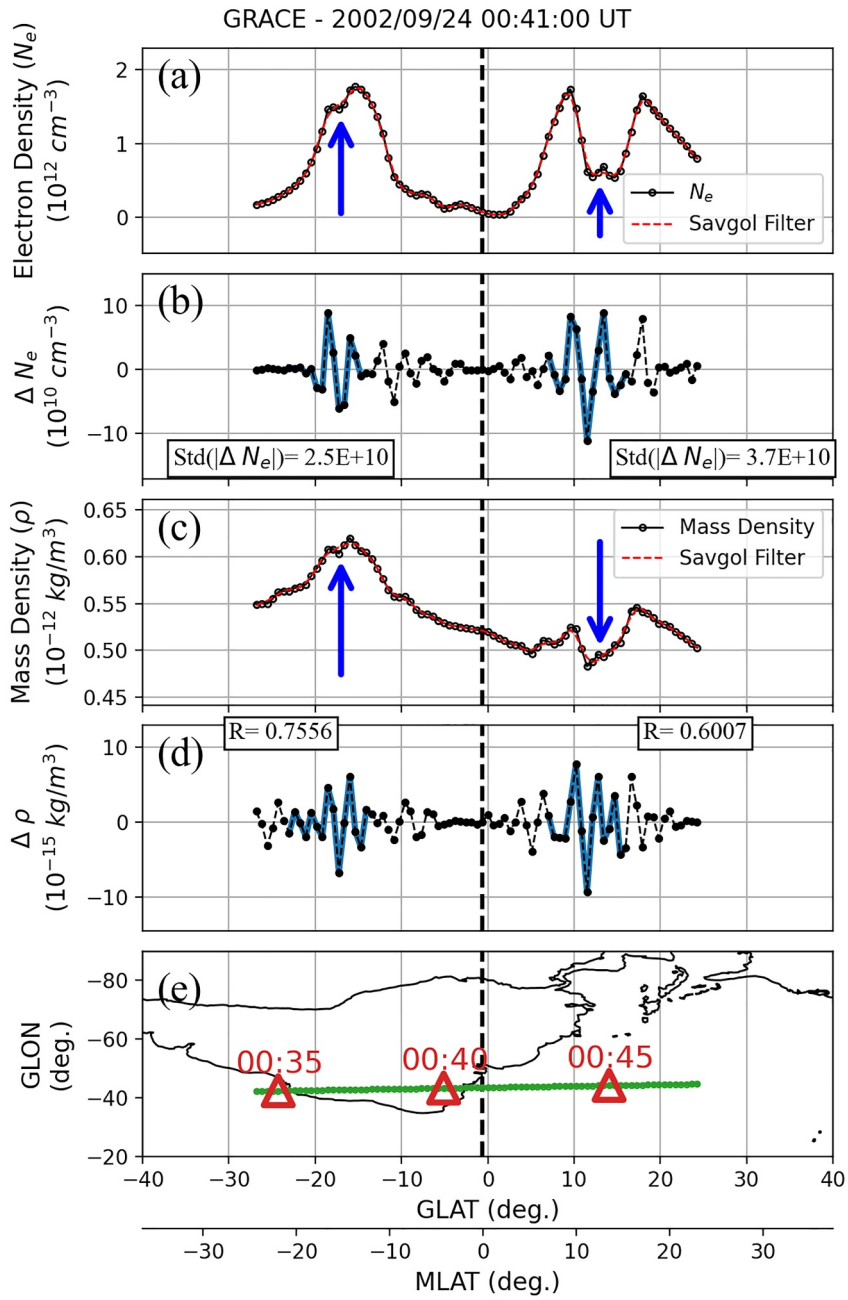

Figure 1. An example of electron and neutral density disturbances in Gravity Recovery and Climate Experiment (GRACE) satellite data obtained around 00:41 UT on 24 Sep 2002. The *x*-axis represents the geographic latitude and the magnetic latitude, and the *y*-axis is (a) electron density, (b) electron density residual, (c) neutral density, (d) neutral density residual, and (e) longitude of the ground track of the spacecraft. The magnetic equator on the GRACE pass is drawn with a vertical black dotted line in all the panels. The segment-wise standard deviation of |Δ *Ne*| is displayed in panel (b), and R (correlation coefficient) between panels (b, d) is shown in panel (d). The last panel (e) displays a world map rotated 90° clockwise, with solid black lines.

(e), the *y*-axis is Geographic Longitude (GLON), and the global map rotated clockwise by 90° is drawn with a solid black line. The spacecraft locations are marked with green dots. The red triangles tell us the representative spacecraft positions every 5 min.

The above-mentioned methodology is applied to each "segment," and the resultant residual magnitudes and correlation coefficients are used for detecting EPI and NDD events. The conditions used in the study are

Table 1
Conditions for Equatorial Plasma Irregularitie and Neutral Density Disturbance Detection

Condition	P (EPI)	P (EPI + NDD)
std (|ΔNe|)	$>2 \times 10^9$ cm^{-3}	$>2 \times 10^9$ cm^{-3}
max (|ΔNe|)	$>5 \times 10^9$ cm^{-3}	$>5 \times 10^9$ cm^{-3}
R		>0.45

Note. The standard deviation and maximum value of |ΔNe| are constrained to detect the EPI. A correlation coefficient (R) condition is further added to identify EPI-related NDD.

summarized in Table 1. Given a data "segment," if (a) a segment-wise standard deviation (hereafter, std) of $|\Delta Ne|$ is greater than 2×10^9 cm^{-3} (see the annotations in Figure 1b) and (b) the maximum value of $|\Delta Ne|$ is greater than 5×10^9 cm^{-3}, the segment is judged to contain EPIs and tagged as an EPI segment. Similar event thresholds were used by Xiong et al. (2010). Further, if an EPI segment satisfies the third criterion, such that (c) the correlation coefficient between ΔNe and $\Delta\rho$ (hereafter, R) exceeds 0.45, that "segment" is deemed to contain both EPIs and NDDs: they are hereafter called NDD segments. The threshold of 0.45 is chosen because each correlation window within a segment usually consists of 15 data points (or 150 s composed of ±70s and the center point) and the correlation coefficient of 0.45 therein is significant at the $p < 0.1$ level. In summary, conditions for an EPI segment are (a) std($|\Delta Ne|$) $> 2 \times 10^9$ cm^{-3}, and (b) max($|\Delta Ne|$) $> 5 \times 10^9$ cm^{-3}, while an NDD segment fulfills both EPI conditions and also (c) R > 0.45. As a result, the NDD segments are a subset of EPI segments in our analysis: that is, all NDD segments already contain EPIs.

3. Result

Figure 2 shows the S/L distribution of EPI and NDD events, in a format similar to those used by Stolle et al. (2006) and Xiong et al. (2010), both of which addressed EPI climatology. In all panels, the *x*-axis represents Geographic Longitude (GLON), and the *y*-axis represents months (or equivalently, seasons). The color palette is the occurrence rate of EPIs (panel a) or NDDs (panel b) in each bin, multiplied by 100 to express the ratio as a percentage. The rate means the ratio of the number of EPI segments (panel a) or NDD segments (panel b) to the total number of GRACE segments per bin. The bin sizes are 10° in GLON and 10 days in Day-Of-Year (DOY). Figure 2a shows the S/L distribution of EPIs, and it is evident that these results are consistent with past research (Stolle et al., 2006; Xiong et al., 2010). Figure 2b gives the occurrence rate of NDDs in the same format, and the distribution largely follows that of Figure 2a: the EPI-NDD similarity is in general agreement with Park et al. (2010). Figure 2c shows the ratio between Figures 2a and 2b, and hereafter, "EPI-to-NDD efficiency" means the efficiency with which an EPI co-exists with observable NDD. In Figure 2a, a contour line representing ≥15 EPIs per bin is marked with a black solid line, and this same contour is repeated in Figure 2c. This criterion of 15 EPIs corresponds to ∼21% when converted into the EPI occurrence rate. We focus only on the region inside the contour in Figure 2c (i.e., regions of meaningful EPI occurrence) while addressing the efficiency of an EPI in accompanying NDDs. Outside the contour, EPIs are inherently rare, making the statistical analysis of the efficiency of EPIs accompanying NDDs potentially misleading or unreliable. Inside the contour in Figure 2c, EPIs can be seen to go with NDDs observable by GRACE; see the color palette of Figure 2c. This contour will be referenced again later in the Discussion Section and Figure 7.

Figures 3a and 3b show the occurrence rate of EPI and NDD, respectively, as a function of MLT. In Figures 3a and 3b, all the "segments" used for Figures 2a and 2b are sorted into different MLT bins. Figure 3c presents a simple bin-by-bin division of Figures 3b by 3a: that is, the EPI-to-NDD efficiency. The error bars are calculated as $\sqrt{p(1-p)/n}$. (As for Figures 3a and 3b, the p is the occurrence rate of EPI and NDD, while the n is the number of "segments" in each bin. In Figure 3c, the p represents the EPI-to-NDD efficiency, and the n represents the number of "EPI segments" per bin.) Note that the MLT 18:00 bin corresponds to the MLT range between 18:00 and 19:00 LT. For 20 years of data from 2002 to 2022, the EPI occurrence rate (Figure 3a) rapidly decays after 22:00 LT at GRACE altitude (Xiong et al., 2010). Data after 04:00 LT are excluded, following previous studies (Stolle et al., 2006; Xiong et al., 2010). In Figure 3b, the NDD occurrence rate peaks around 22:00 MLT, which is in broad agreement with Park et al. (2010; Figure 2). In Figure 3c, the time at which NDD is frequently collocated with EPIs is about 20:30-02:30 LT. In other words, although a small dip (by ∼5%) exists around 23:00 LT, the EPI-to-NDD efficiency is overall high around midnight and generally decreases toward the dawn and dusk sectors.

Figure 4 shows the connection between EPIs and NDDs by solar activity. Similar to Figures 2 and 3, panel (a) of Figure 4 presents the EPI occurrence rate, panel (b) presents the NDD occurrence rate, and panel (c) shows the simple bin-by-bin ratio between panels (b) and (a). The bin averages are shown as black dots plotted against the solar F10.7 index (Tapping, 2013). For context, the total number of segments per bin is plotted in blue, with its

10.1029/2023SW003851

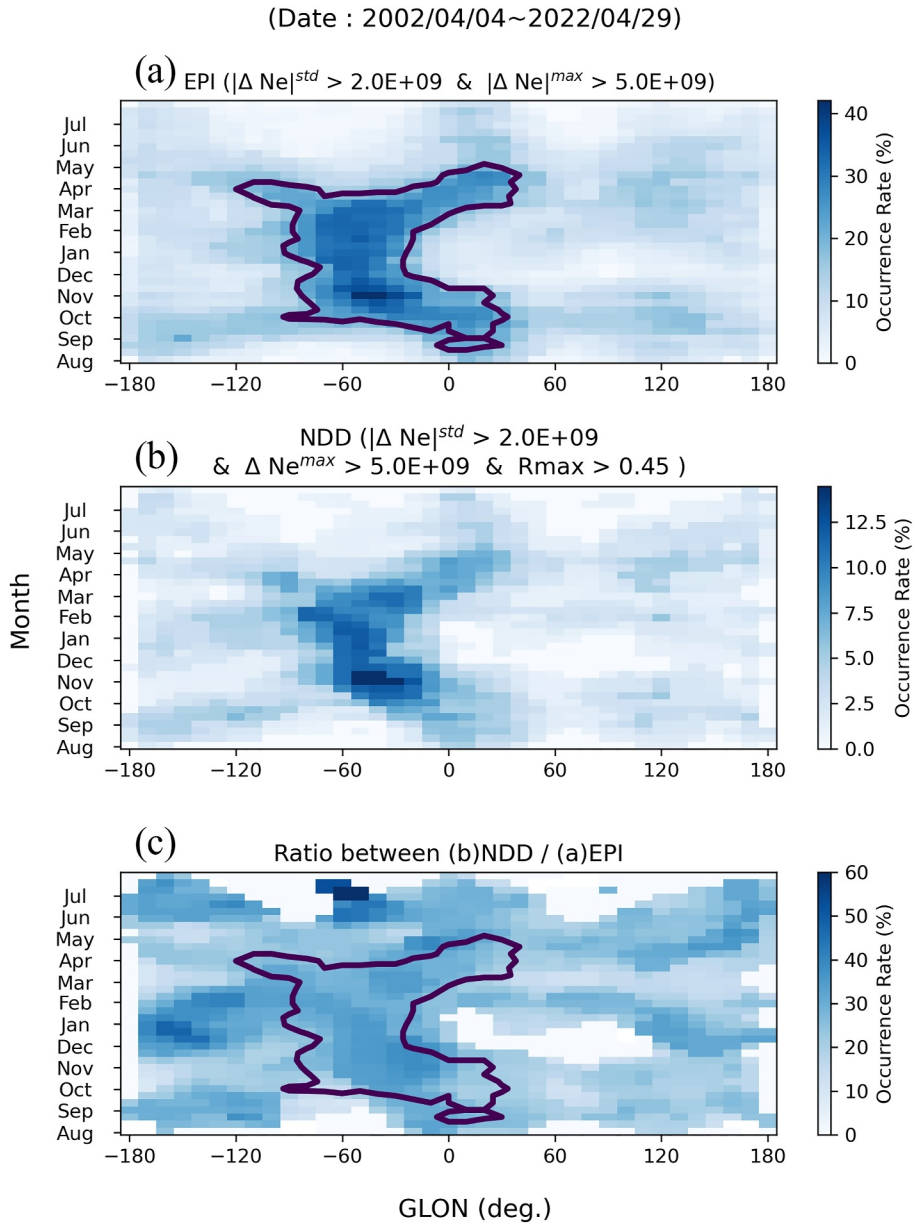

Figure 2. The seasonal/longitudinal (S/L) distribution of equatorial plasma irregularitie (EPI) and Neutral density disturbance (NDD) occurrence rate from Gravity Recovery and Climate Experiment/GRACE-FO data. Panel (a) is a distribution of EPIs, and panel (b) is for NDDs. Panel (c) shows the ratio between panels (a, b) (i.e., the efficiency for an EPI to go with NDDs). The *x*-axis represents GLON, and the *y*-axis represents the months. The color palette indicates the occurrence rate, which is multiplied by 100 to express the ratio as a percentage. The contour drawn with a solid black line represents ≥15 EPIs per bin. This criterion corresponds to ∼21% when converted into the probability of EPI occurrence.

axis shown to the right of each panel. For bins containing more than 3,000 segments, red halos are added to the black dots, which are used for a linear fit that is displayed as a red dashed line. Note that a slightly lower threshold (2,000 segments) was used by Stolle et al. (2006), and our threshold is slightly more conservative. The linear fit result ("trend line") is indicated in the title of each panel. The dependence of EPI occurrence on solar activity, as shown in Figure 4a, is consistent with past research (Stolle et al., 2006; Xiong et al., 2010), confirming that our approach to EPI detection is valid. The increase in NDD occurrence rate with solar activity, shown in Figure 4b, is also in agreement with Park et al. (2010; Figure 3). On the contrary, Figure 4c shows that the EPI-to-NDD efficiency unexpectedly decreases as solar activity increases, albeit with fluctuations.

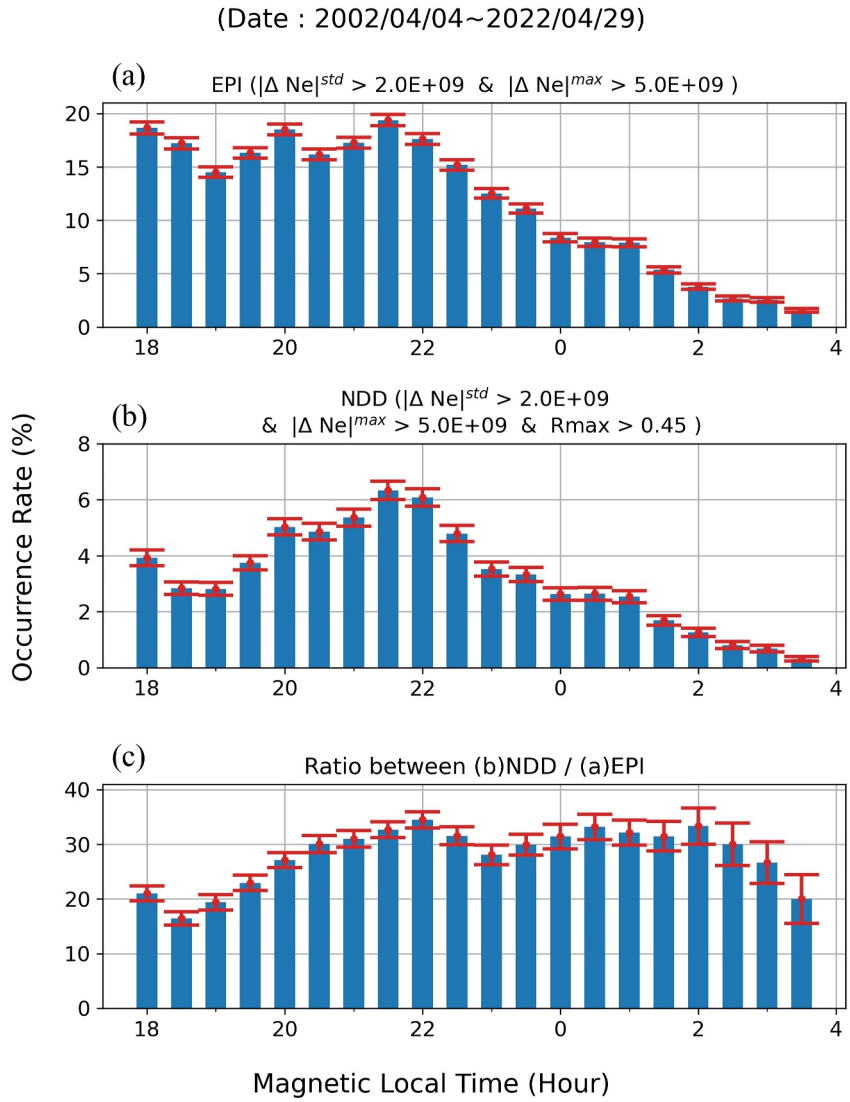

Figure 3. Histogram of occurrence rates of equatorial plasma irregularitie (EPI) and Neutral density disturbance (NDD) as a function of Magnetic Local Time (MLT). Panel (a) presents an EPI occurrence rate, panel (b) that of NDDs, and panel (c) the ratio of (b) to (a), which is the EPI-to-NDD efficiency. The error bars are marked with red solid lines for each bin.

To better understand the relationship between EPI and NDD, we investigate whether EPIs that accompany NDDs have distinct MLAT distributions compared to overall EPIs. For each "segment," we calculate the median MLAT among the data points with a threshold in electron density (i.e., median MLAT of data satisfying $|\Delta Ne| > 2 \times 10^9$ cm^{-3} condition). The segment-wise median MLAT is considered the representative MLAT of plasma density irregularities, and their histograms are shown as blue dash-dot lines in Figure 5a (for EPI segments) and Figure 5b (for NDD segments, i.e., a subset of EPI segments that accompany NDD). The x-axis has a bin size of 1° in MLAT, and the y-axis represents the number of segments. The red dash-plus lines represent the Gaussian fitting curves. The parameters for the red Gaussian fit curve ($A\, e^{-(x-x_0)^2/2\sigma^2}$) in each panel are described in the panel titles. According to Figure 5 and the Gaussian fit equations in the panel titles, there is no significant difference between Figures 5a and 5b. In other words, EPIs that accompany NDDs do not have MLAT distributions that differ significantly from those of overall EPIs.

In this paragraph, we discuss whether strong NDDs are accompanied by strong EPIs. Figure 6 shows the relationship between max($|\Delta Ne|$) and max($|\Delta\rho|$) for each "segment." Figure 6 includes only the NDD segments: that is, only the "segments" exhibiting a significant correlation between ΔNe and $\Delta\rho$ profiles. The main graph is a 2-dimensional

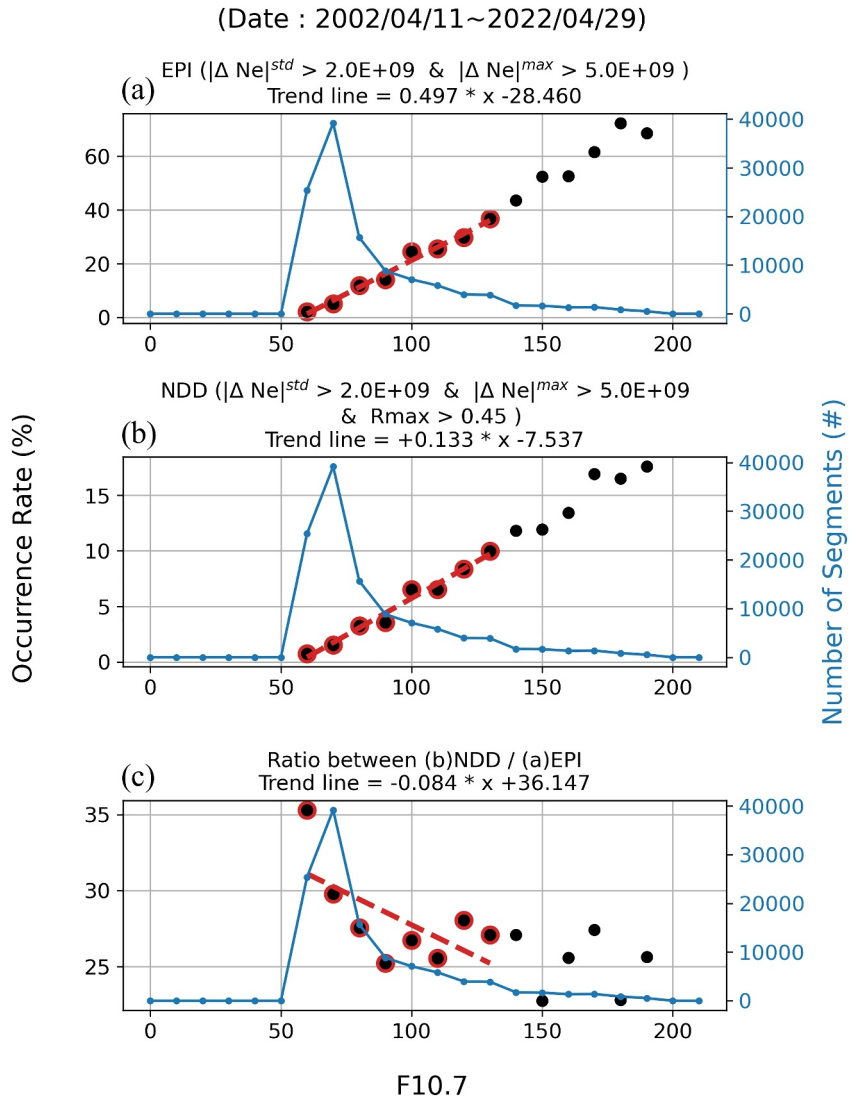

Figure 4. Occurrence rate of equatorial plasma irregularitie (a), Neutral density disturbance (b), and the ratio of the latter to the former (c) as a function of solar activity. Bin averages are shown as black dots. The second blue *y*-axis on the right side of each panel is the total number of segments. Black dots with more than 3,000 segments have red halo. Trend lines are fit only to the data points with a red halo.

histogram with max(|Δρ|) on the *x*-axis and max(|Δ*Ne*|) on the *y*-axis, and the color bar represents the bin population (i.e., number of "segments") in log scale. The 1-dimensional histogram at the top shares the *x*-axis scale with the 2-dimensional histogram, and the histogram at the right shares the *y*-axis scale with the scatter plot. Figure 6 demonstrates that the correlation between max(|Δ*Ne*|) and max(|Δρ|) is weak, especially in the yellow regions (i.e., regions with high bin populations). This poor correlation is generally consistent with a previous study using CHAMP satellite data (Park et al., 2010). In summary, strong NDDs are not necessarily attributed to strong EPIs.

4. Discussion

In this section, we investigate whether the EPI-to-NDD efficiency (as shown in Figure 2c) is higher under a dense (high-density) or tenuous (low-density) thermosphere. Specifically, we record the median of the measured (unfiltered) neutral mass density of each EPI segment and investigate the specific neutral density conditions under which an EPI segment is likely to be co-located with NDD. Note that the median neutral density mentioned in the preceding sentence is not the residual that has been discussed so far (i.e., Δρ), but represents a large-scale background property (ρ_{median}). All four panels in Figure 7 present the distribution of the median neutral density (ρ_{median})

10.1029/2023SW003851

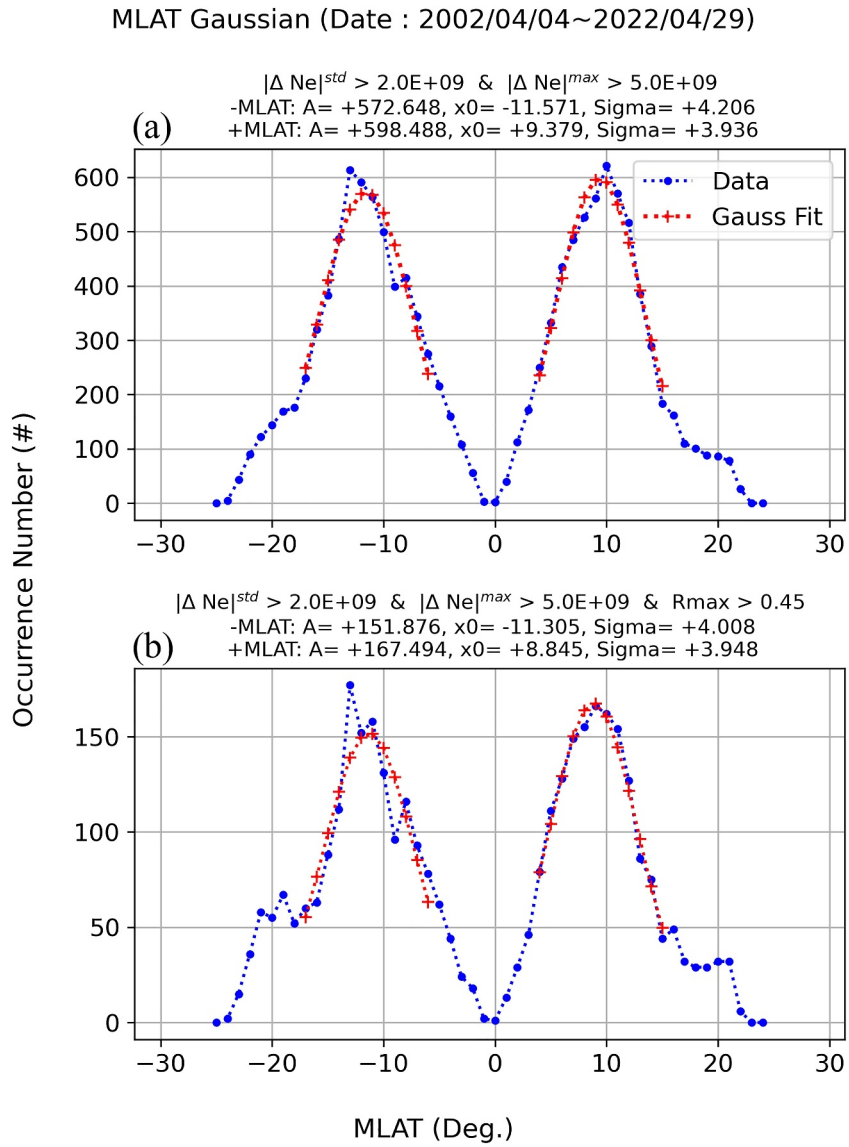

Figure 5. The *x*-axis is MLAT, and the *y*-axis is the histogram of (a) equatorial plasma irregularitie "segments" and (b) Neutral density disturbance "segments" (blue color). Each "segment" is assigned to the MLAT bin that corresponds to the median MLAT among the data points with a threshold of electron density (i.e., median MLAT of data satisfying $|\Delta Ne| > 2 \times 10^9$ cm^{-3} condition). The equations for Gaussian fitting curves (red color) are annotated in the titles of the panels.

in formats similar to the preceding figures. Figure 7a is similar to Figure 2c (i.e., S/L distribution), but presents the median neutral density (ρ_{median}) instead of the EPI-to-NDD efficiency. The black solid contour remains the same from Figure 2c, indicating ≥15 EPIs per bin. Figure 7b is similar to Figure 3c (i.e., MLT dependence), but again for the median neutral density (ρ_{median}). Figure 7b bears a general resemblance to the thermosphere climatology reported by Liu et al. (2005; Figures 2 and 8), but is slightly different from it. We note that Figure 7 represents only the neutral mass density (ρ_{median}) of the "EPI segments" while Liu et al. (2005) were free from such a constraint. By comparing Figure 3c (EPI-to-NDD efficiency of EPI segments vs. MLT) and Figure 7b (ρ_{median} of EPI segments vs. MLT), we can find that the EPI-to-NDD efficiency generally increases when ρ_{median} is low (e.g., around midnight). This trend is identifiable even in the S/L distribution: Figure 7c, which is the correlation diagram between the EPI-to-NDD efficiency (from inside the black contour of Figure 2c) and ρ_{median} (from inside the black contour of Figure 7a) in the S/L distribution, clearly exhibits a negative correlation between the former and the latter. To corroborate the negative correlation in Figure 7c, we replaced the ≥15-event threshold (see Figure 7a) with other values, such as 10 and 20 EPIs per bin, and the negative correlation persists: −0.316 for the 10-event threshold and

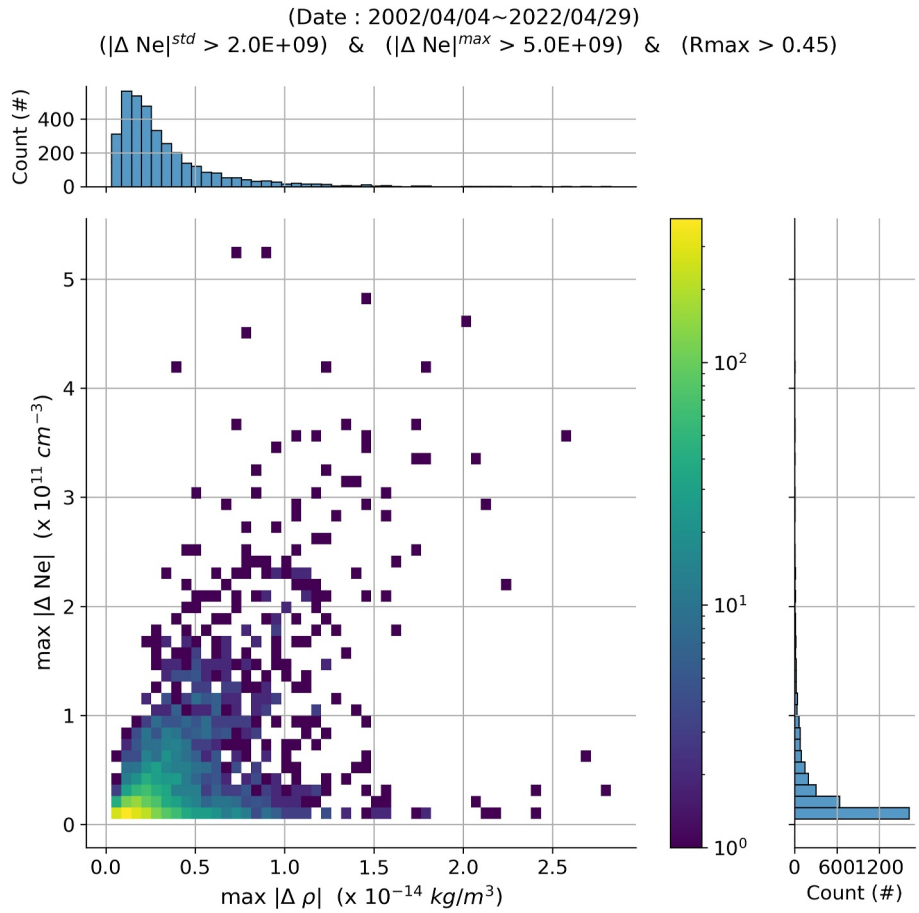

Figure 6. The biggest graph is a 2-dimensional histogram between max(|Δ*Ne*|) and max(|Δρ|) of Neutral density disturbance segments. The *x*-axis represents max(|Δ ρ|), the *y*-axis represents max(|Δ*Ne*|), and the color bar displays the bin population on a log scale. There are 2 smaller panels on the top and right of the main graph, which correspond to the 1-dimensional histogram of the same data set.

−0.581 for the 20-event threshold. This evidence shows that EPI-to-NDD efficiency is higher when background thermospheric density (ρ_{median}) is low: that is, cold thermosphere (see Park, Evans, et al., 2022; Figure 6). Figure 7d is similar to Figure 4, but presents ρ_{median} as a function of solar activity. The ρ_{median} trend in this figure is in the opposite direction of the EPI-to-NDD efficiency trend with solar activity shown in Figure 4c, again indicating a negative correlation between the EPI-to-NDD efficiency and ρ_{median}.

The negative correlation between EPI-to-NDD efficiency and ρ_{median} can be interpreted as an effect of neutral fluid advection in the presence of a vertical density gradient (Newton & Pelz, 1973). Around the altitude of the peak density of electrons in the ionosphere, though the plasma density is only about 0.1% of the neutral density, it can significantly influence the neutral atmosphere (Hussien et al., 2020; Jee, 2023). Figure 8 shows a conceptual sketch explaining the difference in the updraft of neutral species inside and outside of an EPI. As the ion-neutral collision frequency differs inside and outside EPIs, the updraft of neutral species affected by ionospheric plasma should also differ, which is expected to be the source of NDDs (Hanson & Bamgboye, 1984; Ieda, 2020). The inhomogeneous updraft of neutral species should leave imprints in the neutral density profile at a fixed altitude, such as in the GRACE(-FO) data, due to the advection effect. The advection effect is expressed in Equation 1:

$$\frac{\partial \rho}{\partial t} + \nabla \cdot (\rho \boldsymbol{u}) = \frac{\partial \rho}{\partial t} + \boldsymbol{u} \cdot \nabla \rho + \rho \nabla \cdot \boldsymbol{u} = 0 \quad (1)$$

where ρ is neutral density and $\boldsymbol{u}$ is the velocity field of neutral species. Assuming incompressible neutral fluid for simplicity ($\nabla \cdot \boldsymbol{u} = 0$), the change in neutral density ($\frac{\partial \rho}{\partial t}$) is proportional to the dot product of velocity ($\boldsymbol{u}$) and

10.1029/2023SW003851

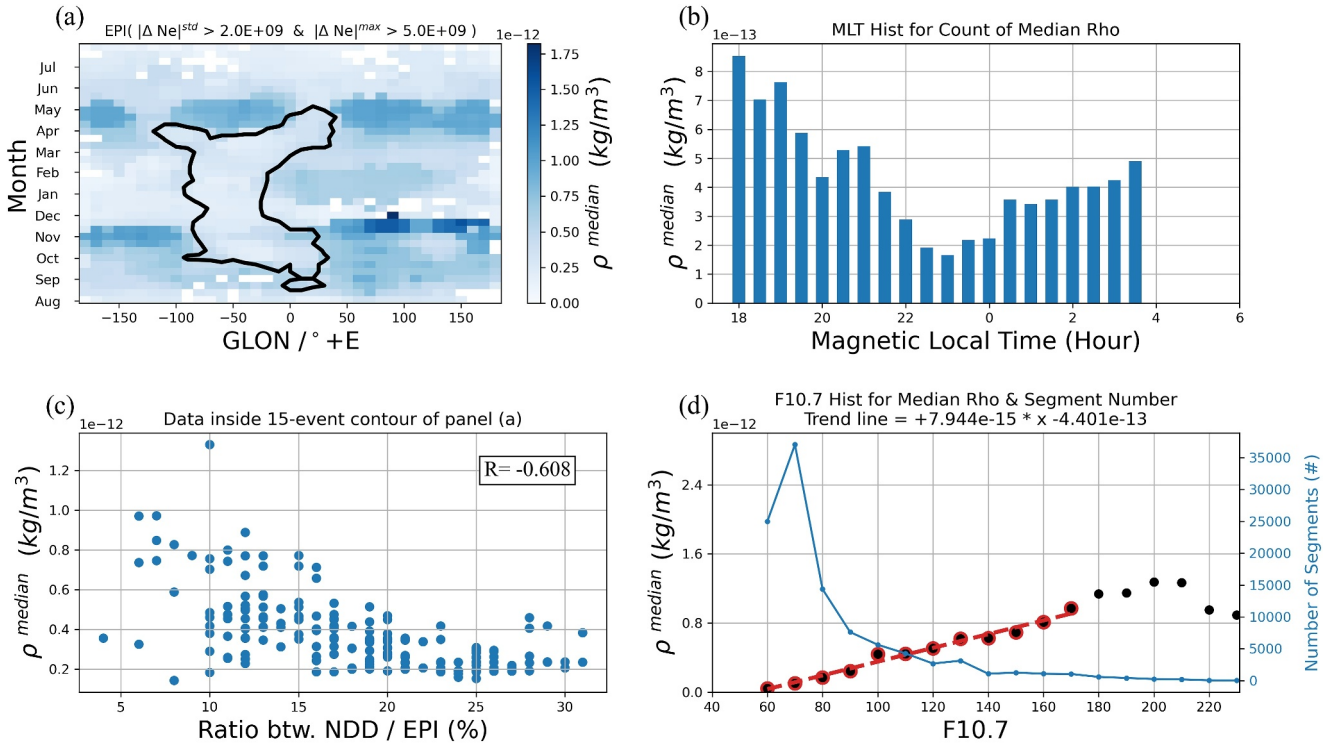

Figure 7. Distribution of segment-wise median of neutral density (ρ_{median}) of all the equatorial plasma irregularitie (EPI) segments. Panel (a) is a picture similar to Figure 2c: the *x*-axis is longitude, and the *y*-axis is months, while the color bar is ρ_{median}. Panel (b) is a histogram for MLT, which is similar to Figure 3c, but the *y*-axis is again ρ_{median}. Panel (c) shows the correlation diagram between Figure 2c (EPI-to-NDD efficiency) and (a) (ρ_{median}), for each bin within the black solid contour in Figure 2c. Panel (d) is a similar graph to Figure 4c, but the *y*-axis is ρ_{median}. The black solid contours represent ≥15 EPIs per bin, which is the same as in Figure 2c.

gradient of the neutral species ($\nabla\rho$). Therefore, given an upward velocity u_z, the concomitant density change is expected to increase when the vertical gradient of ρ ($=|\nabla\rho|_z$) is large (equivalently, when the scale height of the neutral density is small).

A smaller scale height of neutral species generally indicates lower background neutral density (e.g., lower ρ_{median} in Figure 7), because the neutral species in the terrestrial thermosphere can be approximated by an exponential function with a scale height (H):

$$\rho = \rho_0 e^{-z/H} \tag{2}$$

where z is the height with respect to a reference height, and ρ_0 is the neutral density at that reference height. Therefore, if an EPI induces an inhomogeneous updraft of ambient thermospheric neutral species, the resultant density changes of neutrals would be greater when the neutral scale height is small, or equivalently, when the thermospheric density is low, such as during solar minima (Thayer et al., 2012; Xiong et al., 2018; Yang et al., 2022). In Figure 9, we compare the scale height during solar maximum (blue circles) and solar minimum (red crosses) using the Mass Spectrometer and Incoherent Scatter model (MSIS) model of version 2.0 (Emmert et al., 2021). The black horizontal dotted line indicates the nominal altitude of the GRACE satellite at 500 km. The scale height is greater during the solar maximum than in the solar minimum. This advection effect driven by EPIs, in combination with background neutral scale heights, which depends on S/L, MLT, and solar activity, may explain the anti-correlation between EPI-to-NDD efficiency and background neutral density (ρ_{median}), as shown in Figure 7c. Additionally, the scale height effect may also explain the poor correlation between max($|\Delta Ne|$) and max($|\Delta\rho|$) in Figure 6, as $\Delta\rho$ is not only affected by the $|\Delta Ne|$ (i.e., spatially inhomogeneous ion-to-neutral momentum transfer) but is also controlled by the neutral density scale height (see Equation 1).

As a final remark, we note that though the ionospheric plasma makes up only a small part of the thermospheric mass density, it might be able to drive observable thermospheric depletion. At least two previous simulation studies

10.1029/2023SW003851

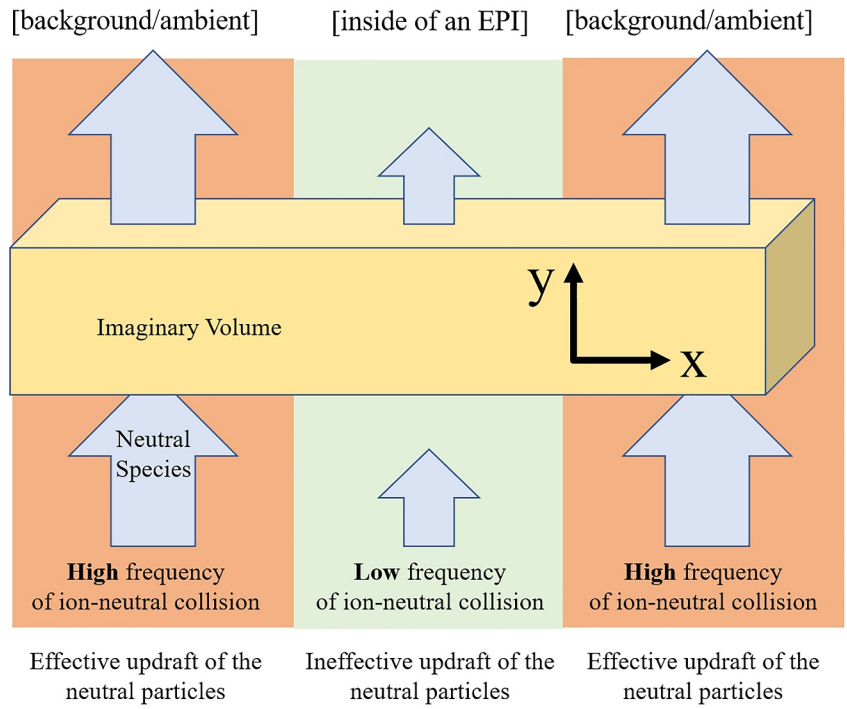

Figure 8. Differences in the updraft of neutral species inside and outside an equatorial plasma irregularitie (EPI). The middle green region represents the interior of the EPI, while the orange regions on its left and right correspond to the exterior of the EPI. The yellow box represents an imaginary volume to show the divergence-free nature of the neutral flow, with the *x* and *y* coordinates indicating the zonal and vertical directions, respectively. The blue arrows signify updrafting neutral species: the stronger the vertical flow, the larger the arrow.

successfully demonstrated that EPI can cause NDD. Bencze et al. (2000) argued, based on their modeling result (e.g., Figure 11), that the origin of NDD is EPI. Schunk and Demars (2003) also stated that their simulation results support the hypothesis that EPI causes NDD, and we could not find any other publications that refute this argument. However, neither the simulations of Bencze et al. (2000) nor those of Schunk and Demars (2003) can provide a fully quantitative explanation for the GRACE(-FO) results presented in this paper. This is because the EPIs assumed in those numerical studies had an extreme depth of about 99%, while the resultant NDDs strengths were only a few percent. Therefore, the two simulation studies can only be considered as references rather than quantitative evidence. Ultimately, further studies should be conducted to provide a detailed analysis of EPIs and NDDs, aiming to uncover the origin of their locations.

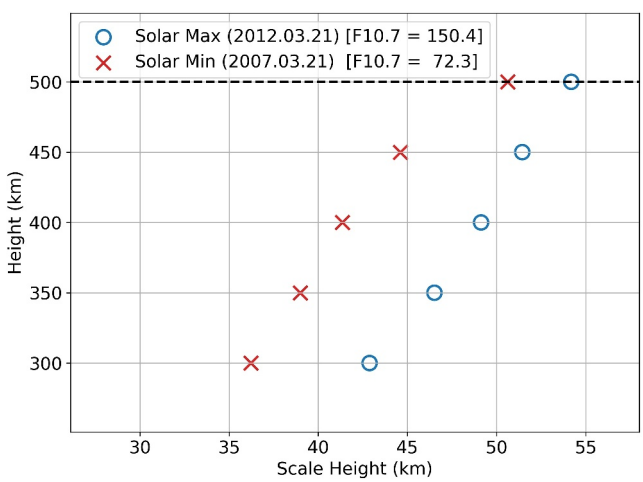

Figure 9. Altitude profile for neutral density scale height. The *x*-axis represents the scale height, and the *y*-axis is the height. The horizontal black dotted line indicates the altitude of 500 km, which is the nominal altitude of GRACE(-FO) satellites. The blue circles represent the neutral density scale height of the solar maximum (2012), and the red crosses represent that of the solar minimum (2007). The date is based on the spring equinox (March 21), local time of 20:00, and MLAT of 10°.

5. Conclusions

In this study, we analyzed the association between EPI and NDD at altitudes between 450 and ~500 km using electron and neutral density simultaneously measured by the GRACE/GRACE-FO satellites over nearly two decades. The dependences of EPI and NDD on season/longitude (S/L), MLT, and the solar cycle were addressed, and the main findings of this study can be summarized as follows:

1. EPI-related NDD climatology is reported at altitudes above 450 km for the first time. The S/L distribution and the dependences on MLT and solar activity are generally consistent with previous NDD studies at lower altitudes.
2. In this study, NDDs are identified through the correlation analysis between electron and neutral density profiles obtained quasi-simultaneously at the

same satellite. This method is robust against possible contaminations of (a) noise and (b) NDDs unrelated to EPIs (e.g., gravity waves originating from the lower atmosphere).

3. We find an anti-correlation between EPI-to-NDD efficiency and background neutral density (ρ_{median}). This trend indicates that the probability of EPIs co-existing with observable NDDs increases as background neutral density decreases. We suggest that these observations can be explained by inhomogeneous neutral species advection induced by EPIs, which would cause inhomogeneous neutral density at a fixed altitude, especially when the background neutral density exhibits a steep vertical gradient (i.e., when the background neutral density is low).

Data Availability Statement

The electron density (*Ne*) and neutral density (ρ) data of GRACE/GRACE-FO satellites can be accessed from the official website of ESA (https://swarm-diss.eo.esa.int). The *Ne* data directory is "Home/Multimission/GRACE/NE/Dual_Sat" for GRACE, and "Home/Multimission/GRACE-FO/NE/Dual_Sat" for GRACE-FO. The ρ data directory is "Home/Multimission/GRACE/DNS/Sat_1" for GRACE, and "Home/Multimission/GRACE-FO/DNS/Sat_1" for GRACE-FO.

Acknowledgments
This research was supported by the Korea Astronomy and Space Science Institute under the R&D program (Project No. 2024-1-850-02) supervised by the Ministry of Science and ICT. PJ was supported by the National Research Council of Science & Technology (NST) grant by the Korean government (MSIT; No. CPS21161-120). We acknowledge the Community Coordinated Modeling Center (CCMC) at Goddard Space Flight Center for the use of the NRLMSIS (Mass Spectrometer and Incoherent Scatter model), "https://ccmc.gsfc.nasa.gov/models/NRLMSIS~00/." We acknowledge the use of ApexPy Version 2.0.1, which can be accessed via this link (https://doi.org/10.5281/zenodo.7818719).

References

Aa, E., Zou, S., & Liu, S. (2020). Statistical analysis of equatorial plasma irregularities retrieved from Swarm 2013–2019 observations. *Journal of Geophysical Research: Space Physics*, *125*(4). https://doi.org/10.1029/2019JA027022

Behzadpour, S., Mayer-Gürr, T., & Krauss, S. (2021). GRACE follow-on accelerometer data recovery. *Journal of Geophysical Research: Solid Earth*, *126*(5). https://doi.org/10.1029/2020JB021297

Bencze, P., Almã Ar, I., & Illã Es-Almã Ar, E. (2000). Further results referring to the neutral density depletions attributed to plasma bubbles. *Journal of Atmospheric and Solar-Terrestrial Physics*, *62*(15), 1339–1350. https://doi.org/10.1016/s1364-6826(00)00149-8

Burke, W. J., Gentile, L. C., Huang, C. Y., Valladares, C. E., & Su, S. Y. (2004). Longitudinal variability of equatorial plasma bubbles observed by DMSP and ROCSAT-1. *Journal of Geophysical Research*, *109*(A12). https://doi.org/10.1029/2004JA010583

Christophe, B., Boulanger, D., Foulon, B., Huynh, P. A., Lebat, V., Liorzou, F., & Perrot, E. (2015). A new generation of ultra-sensitive electrostatic accelerometers for GRACE Follow-on and towards the next generation gravity missions. *Acta Astronautica*, *117*, 1–7. https://doi.org/10.1016/j.actaastro.2015.06.021

Emmert, J. T., Drob, D. P., Picone, J. M., Siskind, D. E., Jones, M., Mlynczak, M. G., et al. (2021). NRLMSIS 2.0: A whole-atmosphere empirical model of temperature and neutral species densities. *Earth and Space Science*, *8*(3). https://doi.org/10.1029/2020EA001321

Emmert, J. T., Richmond, A. D., & Drob, D. P. (2010). A computationally compact representation of magnetic-apex and Quasi-Dipole coordinates with smooth base vectors. *Journal of Geophysical Research*, *115*(8). https://doi.org/10.1029/2010JA015326

Fejer, B. G., Scherliess, L., & de Paula, E. R. (1999). Effects of the vertical plasma drift velocity on the generation and evolution of equatorial spread F. *Journal of Geophysical Research*, *104*(A9), 19859–19869. https://doi.org/10.1029/1999ja900271

Hanson, W. B., & Bamgboye, D. K. (1984). The measured motions inside equatorial plasma bubbles. *Journal of Geophysical Research*, *89*(A10), 8997–9008. https://doi.org/10.1029/JA089iA10p08997

Huang, C. S., De La Beaujardiere, O., Roddy, P. A., Hunton, D. E., Liu, J. Y., & Chen, S. P. (2014). Occurrence probability and amplitude of equatorial ionospheric irregularities associated with plasma bubbles during low and moderate solar activities (2008-2012). *Journal of Geophysical Research: Space Physics*, *119*(2), 1186–1199. https://doi.org/10.1002/2013JA019212

Huang, C. Y., Burke, W. J., Machuzak, J. S., Gentile, L. C., & Sultan, P. J. (2002). Equatorial plasma bubbles observed by DMSP satellites during a full solar cycle: Toward a global climatology. *Journal of Geophysical Research*, *107*(A12). SIA 7-1-SIA 7-10. https://doi.org/10.1029/2002JA009452

Huang, F., Lei, J., Xiong, C., Zhong, J., & Li, G. (2021). Observations of equatorial plasma bubbles during the geomagnetic storm of October 2016. *Earth and Planetary Physics*, *5*(5), 1–11. https://doi.org/10.26464/epp2021043

Hussien, F., Ghamry, E., Fathy, A., & Mahrous, S. (2020). Swarm satellite observations of the 21 August 2017 solar eclipse. *Journal of Astronomy and Space Sciences*, *37*(1), 29–34. https://doi.org/10.5140/JASS.2020.37.1.29

Ieda, A. (2020). Ion-neutral collision frequencies for calculating ionospheric conductivity. *Journal of Geophysical Research: Space Physics*, *125*, e2019JA027128. https://doi.org/10.1029/2019JA027128

Illés-Almár, E., Almár, I., & Bencze, P. (1998). Neutral density depletions attributed to plasma bubbles. *Journal of Geophysical Research*, *103*(A3), 4115–4116. https://doi.org/10.1029/97ja02963

Jee, G. (2023). Fundamentals of numerical modeling of the mid-latitude ionosphere. *Journal of Astronomy and Space Sciences*, *40*(1), 11–18. https://doi.org/10.5140/jass.2023.40.1.11

Kelley, M. C. (2009). *The Earth's ionosphere plasma physics and electrodynamics* (2nd ed.). Academic Press.

Kil, H. (2015). The morphology of equatorial plasma bubbles - A review. *Journal of Astronomy and Space Sciences*, *32*(1), 13–19. https://doi.org/10.5140/JASS.2015.32.1.13

Kil, H. (2022). The occurrence climatology of equatorial plasma bubbles: A review. *Journal of Astronomy and Space Sciences*, *39*(2), 23–33. https://doi.org/10.5140/JASS.2022.39.2.23

Kim, J., & Lee, S. W. (2009). Flight performance analysis of GRACE K-band ranging instrument with simulation data. *Acta Astronautica*, *65*(11–12), 1571–1581. https://doi.org/10.1016/j.actaastro.2009.04.010

Klinger, B., & Mayer-Gürr, T. (2016). The role of accelerometer data calibration within GRACE gravity field recovery: Results from ITSG-Grace2016. *Advances in Space Research*, *58*(9), 1597–1609. https://doi.org/10.1016/j.asr.2016.08.007

Kuai, J., Wang, K., Zhong, J., Wan, X., Huang, F., Sun, H., et al. (2022). Analysis of the ionospheric irregularities and phase scintillation at low and middle latitudes based on Swarm observations. *Remote Sensing*, *14*(19), 4780. https://doi.org/10.3390/rs14194780

Landerer, F. W., Flechtner, F. M., Save, H., Webb, F. H., Bandikova, T., Bertiger, W. I., et al. (2020). Extending the global mass change data record: GRACE follow-on instrument and science data performance. *Geophysical Research Letters*, *47*(12). https://doi.org/10.1029/2020GL088306

Liu, H., Lühr, H., Henize, V., & Köhler, W. (2005). Global distribution of the thermospheric total mass density derived from CHAMP. *Journal of Geophysical Research*, *110*(A4). https://doi.org/10.1029/2004JA010741

Matzka, J., Stolle, C., Yamazaki, Y., Bronkalla, O., & Morschhauser, A. (2021). The geomagnetic Kp index and derived indices of geomagnetic activity. *Space Weather*, *19*(5). https://doi.org/10.1029/2020SW002641

Newton, G. P., & Pelz, D. T. (1973). Neutral thermosphere temperatures from density scale height measurements. *Journal of Geophysical Research*, *78*(4), 725–732. https://doi.org/10.1029/ja078i004p00725

Park, J., Evans, J. S., Eastes, R. W., Lumpe, J. D., van den IJssel, J., Englert, C. R., & Stevens, M. H. (2022). Exospheric temperature measured by NASA-GOLD under low solar activity: Comparison with other data sets. *Journal of Geophysical Research: Space Physics*, *127*(3), e2021JA030041. https://doi.org/10.1029/2021JA030041

Park, J., Lühr, H., & Min, K. W. (2010). Neutral density depletions associated with equatorial plasma bubbles as observed by the CHAMP satellite. *Journal of Atmospheric and Solar-Terrestrial Physics*, *72*(2–3), 157–163. https://doi.org/10.1016/j.jastp.2009.11.003

Park, J., Mende, S. B., Eastes, R. W., & Frey, H. U. (2022). Climatology of equatorial plasma bubbles in ionospheric connection explorer/far-UltraViolet (ICON/FUV) Limb Images. *Journal of Astronomy and Space Sciences*, *39*(3), 87–98. https://doi.org/10.5140/JASS.2022.39.3.87

Park, J., Min, K. W., Kim, V. P., Kil, H., Su, S.-Y., Chao, C. K., & Lee, J.-J. (2008). Equatorial plasma bubbles with enhanced ion and electron temperatures. *Journal of Geophysical Research*, *113*(A9). https://doi.org/10.1029/2008JA013067

Park, J., Stolle, C., Yamazaki, Y., Rauberg, J., Michaelis, I., & Olsen, N. (2020). Diagnosing low-/mid-latitude ionospheric currents using platform magnetometers: CryoSat-2 and GRACE-FO. *Earth Planets and Space*, *72*(1), 162. https://doi.org/10.1186/s40623-020-01274-3

Park, J., van den IJssel, J., & Siemes, C. (2023). Dayside upper-thermospheric density fluctuations as observed by GRACE and GRACE-FO at ~500 km height. *Journal of Geophysical Research: Space Physics*, *128*(1). https://doi.org/10.1029/2022JA030976

Schreiter, L., Stolle, C., Rauberg, J., Kervalishvili, G., van den IJssel, J., Arnold, D., et al. (2023). Topside ionosphere sounding from the CHAMP, GRACE, and GRACE-FO missions. *Radio Science*, *58*(3). https://doi.org/10.1029/2022RS007552

Schunk, R. W., & Demars, H. G. (2003). Effect of equatorial plasma bubbles on the thermosphere. *Journal of Geophysical Research*, *108*(A6). https://doi.org/10.1029/2002JA009690

Siemes, C., Borries, C., Bruinsma, S., Fernandez-Gomez, I., Hładczuk, N., Den IJssel, J., et al. (2023). New thermosphere neutral mass density and crosswind datasets from CHAMP, GRACE, and GRACE-FO. *Journal of Space Weather and Space Climate*, *13*, 623–644. https://doi.org/10.1051/swsc/2023014

Stolle, C., Lühr, H., Rother, M., & Balasis, G. (2006). Magnetic signatures of equatorial spread F as observed by the CHAMP satellite. *Journal of Geophysical Research*, *111*(A2), A02304. https://doi.org/10.1029/2005JA011184

Tapley, B. D., Bettadpur, S., Watkins, M., & Reigber, C. (2004). The gravity recovery and climate experiment: Mission overview and early results. *Geophysical Research Letters*, *31*(9). https://doi.org/10.1029/2004GL019920

Tapping, K. F. (2013). The 10.7 cm solar radio flux (F10.7). *Space Weather*, *11*(7), 394–406. https://doi.org/10.1002/swe.20064

Thayer, J. P., Liu, X., Lei, J., Pilinski, M., & Burns, A. G. (2012). The impact of helium on thermosphere mass density response to geomagnetic activity during the recent solar minimum. *Journal of Geophysical Research*, *117*(7). https://doi.org/10.1029/2012JA017832

van der Meeren, C., Laundal, K. M., Burrell, A. G., Lamarche, L. L., Starr, G., Reimer, A. S., & Morschhauser, A. (2023). aburrell/apexpy: ApexPy Version 2.0.1. *Zenodo*. https://doi.org/10.5281/zenodo.7818719

Whalen, J. A. (2003). Dependence of the equatorial anomaly and of equatorial spread f on the maximum prereversal E × B drift velocity measured at solar maximum. *Journal of Geophysical Research*, *108*(A5). https://doi.org/10.1029/2002JA009755

Wu, K., Xu, J., Yue, X., Xiong, C., Wang, W., Yuan, W., et al. (2020). Equatorial plasma bubbles developing around sunrise observed by an all-sky imager and global navigation satellite system network during storm time. *Annales Geophysicae*, *38*(1), 163–177. https://doi.org/10.5194/angeo-38-163-2020

Xiong, C., Lühr, H., Ma, S., & Schlegel, K. (2015). Validation of GRACE electron densities by incoherent scatter radar data and estimation of plasma scale height in the topside ionosphere. *Advances in Space Research*, *55*(8), 2048–2057. https://doi.org/10.1016/j.asr.2014.07.022

Xiong, C., Lühr, H., Schmidt, M., Bloßfeld, M., & Rudenko, S. (2018). An empirical model of the thermospheric mass density derived from CHAMP satellite. *Annales Geophysicae*, *36*(4), 1141–1152. https://doi.org/10.5194/angeo-36-1141-2018

Xiong, C., Park, J., Lühr, H., Stolle, C., & Ma, S. Y. (2010). Comparing plasma bubble occurrence rates at CHAMP and GRACE altitudes during high and low solar activity. *Annales Geophysicae*, *28*(9), 1647–1658. https://doi.org/10.5194/angeo-28-1647-2010

Xiong, C., Stolle, C., Lühr, H., Park, J., Fejer, B. G., & Kervalishvili, G. N. (2016). Scale analysis of equatorial plasma irregularities derived from Swarm constellation. *Earth Planets and Space*, *68*(1), 121. https://doi.org/10.1186/s40623-016-0502-5

Xiong, C., Stolle, C., Michaelis, I., Lühr, H., Zhou, Y., Wang, H., et al. (2021). Correlation analysis of field-aligned currents from the magnetic measurements of GRACE follow-on mission. *Earth Planets and Space*, *73*(1), 206. https://doi.org/10.1186/s40623-021-01540-y

Yan, Y., Müller, V., Heinzel, G., & Zhong, M. (2021). Revisiting the light time correction in gravimetric missions like GRACE and GRACE follow-on. *Journal of Geodesy*, *95*(5), 48. https://doi.org/10.1007/s00190-021-01498-5

Yang, X., Zhu, X., Weng, L., & Yang, S. (2022). A new exospheric temperature model based on CHAMP and GRACE measurements. In *Remote sensing, remote sensing* (Vol. 14(20), p. 5198). MDPI. https://doi.org/10.3390/rs14205198